Detecting the effect of non-thermal sources on the warm-hot Galactic halo

SANSKRITI DAS [ID][1]

[1]*Kavli Institute for Particle Astrophysics and Cosmology, Stanford University, 452 Lomita Mall, Stanford, CA 94305, USA*

ABSTRACT

We report the first detection of non-thermal broadening of O VII lines in the warm-hot $\approx 10^6$ K circumgalactic medium (CGM) of the Milky Way. We use $z=0$ absorption of O VII Kα, O VII Kβ, and O VIII Kα lines in archival grating data of $b > 15°$ quasar sightlines from *Chandra* and *XMM-Newton*. Non-thermal line broadening is evident in 2/3rd of the sightlines considered, and on average is constrained at 4.6σ significance. Non-thermal line broadening dominates over thermal broadening. We extensively test whether the appearance of non-thermal line broadening could instead be because of multiple thermally broadened velocity components and robustly rule it out. Non-thermal line broadening is more evident toward sightlines at lower galactic latitude indicating the Galactic disk origin of the nonthermal sources. There is weak/no correlation between non-thermal line broadening and the angular separation of sightlines from the Galactic center, indicating that the nuclear region might not be a major source of non-thermal factors.

Keywords: Circumgalactic medium — X-ray astronomy — Quasar absorption line spectroscopy — non-thermal radiation sources — Hot ionized medium — Galaxy evolution — Galaxy environments — Galaxy processes — Milky Way Galaxy – Milky Way Galaxy physics — Milky Way evolution

1. INTRODUCTION

The circumgalactic medium (CGM) is the multiphase gaseous region surrounding the disk of a galaxy and filling up its dark matter halo (Truong et al. 2023). The most massive and volume-filling component of the CGM is expected to be virialized, warm-hot, and diffuse ($\approx 10^6$ K; Spitzer 1956; Fielding et al. 2020). This warm-hot $\gtrsim 10^6$ K gas is observed using the emission and absorption lines of He-like and H-like metal ions, e.g., O VII and O VIII, and free-free continuum emission in X-ray. However, due to the intrinsic difficulties in detecting the warm-hot gas, the warm-hot CGM has been best characterized for the Milky Way (see the review by Mathur 2022).

CGM is expected to be influenced by non-thermal sources, e.g., turbulent motions, cosmic rays, and magnetic fields. Under the assumption of hydrostatic equilibrium, non-thermal sources enhance cooling in the hot gas resulting in the generation of cooler and denser phases to balance the total (thermal and non-thermal) pressure against gravity (Bennett & Sijacki 2020; Ji et al. 2020; Schmidt et al. 2021; van de Voort et al. 2021).

Corresponding author: Sanskriti Das
snskriti@stanford.edu

Thus the presence of non-thermal sources in the warm-hot CGM is a natural indicator of coexistent phase(s) at lower temperatures. However, directly constraining the strength of non-thermal sources in the CGM is extremely challenging. For example, nonthermal emission from cosmic-ray electrons in 144 MHz and magnetic fields using Faraday rotation have been detected in the inner CGM of nearby galaxies (Heesen et al. 2019, 2023), but whether it affects the warm-hot phase is unclear. One observable effect of non-thermal sources is that the velocity dispersion is enhanced and the line broadening of tracer element transitions (e.g., O VII in the warm-hot CGM) is larger than their thermal broadening.

In previous studies of the warm-hot CGM in X-rays, the focus has been to detect the warm-hot $\gtrsim 10^6$ K CGM and identify it as the CGM (i.e., ruling out the sources of confusion), calculate the temperature, column density in absorption (e.g., Nicastro et al. 2002; Williams et al. 2005; Fang et al. 2015; Das et al. 2019b, 2021), emission measure in emission (e.g., Henley et al. 2010; Das et al. 2019a; Gupta et al. 2023), and estimate the baryonic mass (Gupta et al. 2012; Nicastro et al. 2016). In this letter, we take a step forward and attempt to constrain the non-thermal line broadening in the warm-hot CGM.

The letter is structured as follows. We present the analysis in §2, show the results, and discuss the phys-
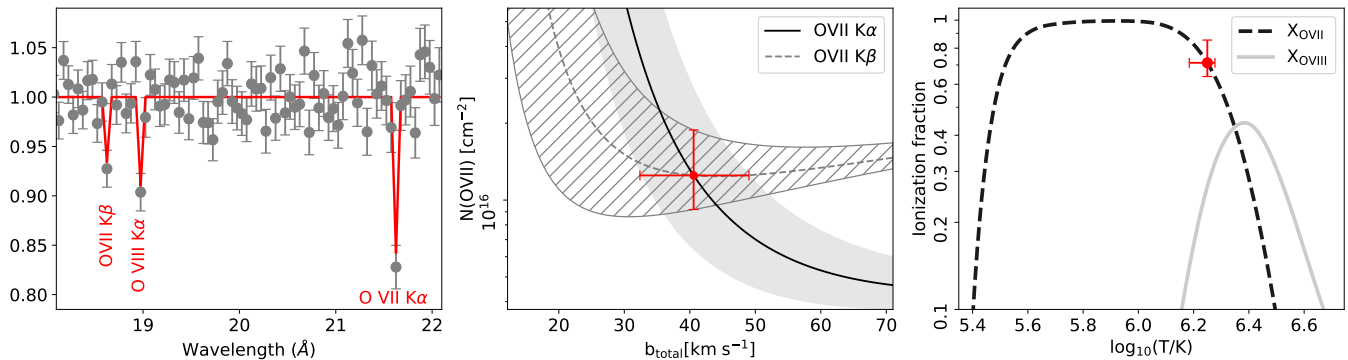
Figure 1. Left: Normalized unfolded spectrum toward one of the sightlines. The $z=0$ absorption lines of O VII Kα, O VII Kβ, and O VIII Kα are shown. Middle: Contours of N(O VII) and total broadening of O VII, b$_{\text{total}}$ for the measured equivalent widths of Kα and Kβ lines toward the same sightline. The saturation-corrected N(O VII) and corresponding b$_{\text{total}}$ are shown with the red point. Right: Ionization fraction of O VII and O VIII, X$_{\text{OVII}}$ and X$_{\text{OVIII}}$, as a function of temperature in collisional ionization equilibrium. The temperature and X$_{\text{OVII}}$ toward the same sightline obtained from the column density ratio of O VIII and O VII (see equation 3b) is shown with the red point.

ical implications in §3. We summarize our results and discuss future directions in §4.

2. METHOD

Our focus is on the warm-hot CGM of the Milky Way. Because oxygen is the most abundant metal in solar-like chemical composition, and O VII and O VIII are the dominant oxygen ions at the temperature of warm-hot phase, we consider the wavelength regions around $z=0$ transitions of O VII Kα, O VII Kβ, and O VIII Kα at 21.602Å, 18.627Å, and 18.978Å. To minimize the contamination by the interstellar medium (ISM), we consider extragalactic quasar sightlines at high galactic latitudes ($b>15°$). We exclude the targets whose blueshifted intrinsic warm absorbers could overlap with $z=0$ lines of our interest. From the *Chandra* archive, we extract all grating data of consideration: 25 HRC/LETG, 14 ACIS/LETG, and 60 ACIS/HETG-MEG sightlines[1], and reduce them with CIAO following standard procedure (see §2.1 of Das et al. 2021). We also consider the quasar sightlines in *XMM-Newton* RGS data published in Nicastro et al. (2016).

To make sure that the O VII Kα line is detectable, we exclude the sightlines with signal-to-noise ratio per resolution element, SNRE<10 around the O VII Kα line. In XSPEC, we fit the continuum with a power law absorbed by the Galactic H I (`tbabs*powerlaw`) and model the oxygen absorption lines with unresolved Gaussian (`agauss`). We freeze N(H I) toward each sightline according to HI4PI Collaboration et al. (2016). We allow the wavelength of the Gaussian lines to vary within the resolution element (50 mÅ for LETG, 25 mÅ for MEG, 70 mÅ for RGS) around the expected $z=0$ values.

To calculate the thermal broadening, we need to constrain the temperature from O VIII and O VII. Therefore we exclude sightlines where O VIII Kα lines are not detected, i.e., where the thermal broadening cannot be estimated. Because the oxygen lines are unresolved, we cannot *directly* measure the total (thermal+non-thermal) line broadening. To *indirectly* calculate the total broadening, both O VII Kα and O VII Kβ lines are required. Therefore we exclude sightlines where O VII Kβ lines are not detected, i.e., where the total broadening cannot be estimated.

If O VII lines are unsaturated, the O VII column density, N, is independent of its total line broadening (Draine 2011). Thus the equivalent width (EW) ratio of O VII Kβ and O VII Kα depends only on the rest-frame transition wavelength, λ, and the oscillator strength[2], f:

$$N = \frac{\pi e^2}{m_e c^2}\frac{EW}{f\lambda^2}$$
$$\frac{EW_{\text{OVII K}\beta}}{EW_{\text{OVII K}\alpha}} = \frac{f_{\text{OVII K}\beta}\lambda^2_{\text{OVII K}\beta}}{f_{\text{OVII K}\alpha}\lambda^2_{\text{OVII K}\alpha}} \tag{1}$$

In this scenario, we cannot estimate the total line broadening and therefore exclude those sightlines for our analysis. We end up with 12 sightlines[3], 7 from *Chandra* and 5 from *XMM-Newton*, where O VII Kα, O VII Kβ, and O VIII Kα lines are detected (Fig. 1, left panel), and the equivalent width ratio of O VII Kβ and O VII Kα is larger than expected from an unsaturated line, indicating saturation of the O VII Kα line.

---

[1] We exclude ACIS data after cycle 14 because of its degradation in soft X-ray

[2] A dimensionless quantity that is a measure of the probability of the transition

[3] Mrk 421 and PKS 2155-304 (ACIS-S/LETG); Mrk 509 and NGC 5548 (HRC-S/LETG); 3C 282, Mrk 290, and NGC 3783 (ACIS-S/HETG-MEG); 1ES 1553+113, 3C 273, 3C 390.3, HE 1029-1401, and PKS 2005-489 (RGS)
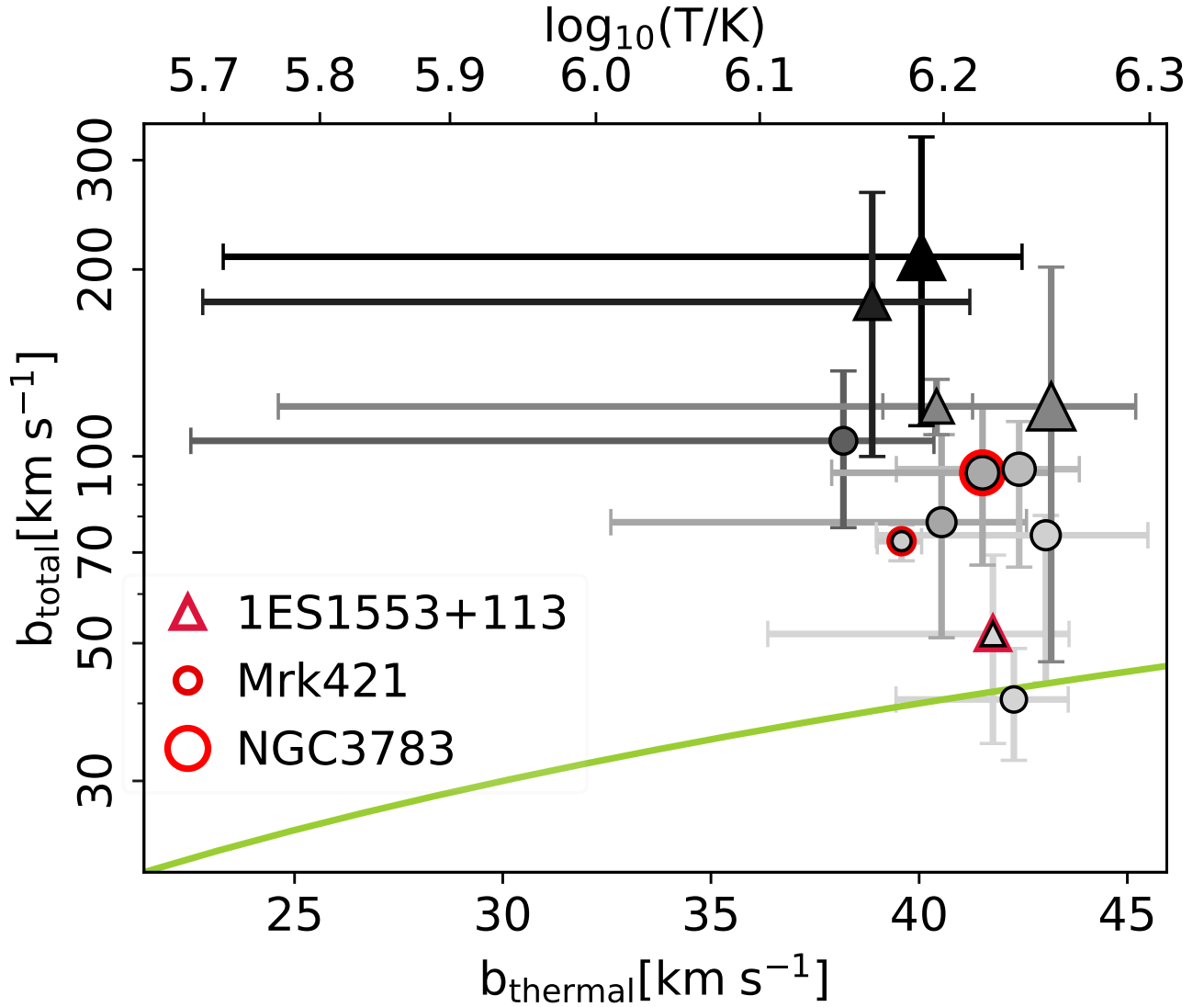
Figure 2. Comparison between thermal and total broadening of O VII lines. The temperature corresponding to the thermal broadening is shown in the upper x-axis. The shade and size of the symbols are proportional to N(O VII) and N(O VIII), respectively, with darker symbols having larger N(O VII) and larger symbols having larger N(O VIII). Measurements from *Chandra* and *XMM-Newton* are shown with circles and triangles, respectively. The green curve denotes the total broadening expected in the absence of non-thermal broadening. In 8 out of 12 sightlines non-thermal broadening is evident. Three sightlines where the presence of a super-virial $\approx 10^7$ K hot phase coexisting with the virial $\approx 10^6$ K warm-hot phase is known, are highlighted in red. The true non-thermal broadening of O VII lines toward these sightlines might be larger than what we measure here in a single phase scenario (see §3.3 for details).

We determine the column density (similar to previous works, e.g., Williams et al. 2005; Gupta et al. 2012) and the total line broadening of O VII as follows. For a saturated but undamped line transition, the column density, N, depends on the equivalent width, EW, of that transition and the total broadening b_{total} (Draine 2011):

$$N = \frac{\ln 2}{\sqrt{\pi}} \frac{m_e c}{e^2} \left(\frac{b_{total}}{f\lambda} \right) exp\left[\left(\frac{cEW}{2b_{total}\lambda} \right)^2 \right] \qquad (2)$$

We construct the contours of N(O VII) vs b_{total}(O VII) for the measured EW values of O VII Kα and O VII Kβ.

We estimate the saturation-corrected N(O VII) and b_{total}(O VII) from where the contours intersect (Fig. 1, middle panel). O VIII Kα line is optically thin and unsaturated, so N(O VIII) is linearly proportional to its EW.

The column density of the i-th ionization state of a metal M, M_i, depends on the column density of hydrogen in that ion-containing phase, N(H), the abundance of that metal to hydrogen, $A_{M/H}$, and the temperature-dependent ionization fraction of that ion, X_{M_i} (equation 3a). Thus, two different ions of the same metal can be used to estimate the temperature of the phase con-

taining those metal ions. Applying this to oxygen, and assuming that all of the O VIII and O VII are coming from a single phase, we can estimate the temperature, T, of that phase (equation 3b; Fig. 1, right panel) from the ratio of N(O VIII) and N(O VII).

$$N(OVII) = N(H)A_{O/H}X_{OVII}(T)$$
$$N(OVIII) = N(H)A_{O/H}X_{OVIII}(T) \quad (3a)$$

$$\frac{N(OVIII)}{N(OVII)} = \frac{X_{OVIII}(T)}{X_{OVII}(T)} \rightarrow T \quad (3b)$$

From the temperature, T, we obtain the thermal broadening of oxygen lines using equation 4:

$$b_{thermal} = \sqrt{\frac{2k_B T}{m_O}} \quad (4)$$

3. RESULTS AND DISCUSSION

We show the total broadening vs thermal broadening of O VII toward all 12 sightlines in Fig. 2. The large uncertainty in the temperature and hence the thermal broadening on the lower end is due to the flattening of the O VII ionization fraction in the temperature range of $10^{5.6-6.2}$ K. The thermal broadening of all sightlines is similar, but the total broadening spans an order-of-magnitude range. In 8 out of 12 sightlines, the total broadening is larger than the thermal broadening including 1σ error, indicating the evidence of non-thermal line broadening.

On average, the thermal and total line broadening are 41^{+1}_{-3} km s^{-1} and 103^{+15}_{-13} km s^{-1}, respectively. It implies a 4.6σ detection of mean non-thermal line broadening of 62^{+15}_{-13} km s^{-1}. The non-thermal broadening is $1.5^{+0.5}_{-0.3}$ times stronger than the thermal broadening.

3.1. Sky distribution

The sightlines we consider are widely spread across the sky (Fig. 3, top panel). None of our sightlines pass through the CGM of M 31, Magellanic Clouds or Magellanic Stream. Therefore, the detection of non-thermal broadening is unlikely to be connected to a special structure in the halo; it could be a general characteristic of the CGM.

We study the variation of O VII line broadening as a function of galactic latitude, longitude, and angle from the Galactic center, $\theta_{center} = \cos^{-1}[\cos(l)\cos(b)]$ in Fig. 3 (bottom panels). To better understand the trend, if any, we average the total broadening into 2 bins of the respective galactic coordinates (red points). The thermal broadening is ≈constant across all sky positions. Thus, any trend of total broadening would be equivalent to that of non-thermal broadening.

Sightlines at smaller galactic longitudes and/or θ_{center} (i.e., inner sightlines) probe the inner CGM that could potentially be affected by the nuclear activity of the Galaxy. Sightlines at larger galactic longitudes and/or

θ_{center} (i.e., outer sightlines) are less/unlikely affected by nuclear activities. At smaller galactic longitudes and θ_{center}, non-thermal line broadening is evident in 3 out of 6 sightlines, which increase to 5 out of 6 sightlines at large galactic longitudes and θ_{center}. The binned total broadening increases by 35% from inner to outer sightlines but is constant within 1σ error. Thus, we do not see any obvious non-thermal effect of (past) nuclear activities on the warm-hot CGM.

Sightlines at lower galactic latitudes are more strongly affected by activities in the Galactic disk. At lower galactic latitudes, non-thermal line broadening is evident in 5 out of 6 sightlines, which decrease to 3 out of 6 sightlines at higher galactic latitudes. The binned total broadening increases by 74^{+64}_{-42}% from higher to lower latitudes. It is consistent with the fact the sources of non-thermal broadening likely originate in the disk.

3.2. Decomposing broadening from velocity

In this section, we discuss if our detection of non-thermal broadening is real, or whether it is a manifestation of multiple thermally broadened components at different velocities.

The line broadening can be directly measured in resolved lines. In that case, the effective linewidth might be overestimated if underlying multiple narrow lines at different velocities are modeled with a single broad line. However, in our case of unresolved lines, we cannot directly measure the linewidth. As described in §2, the total broadening is indirectly measured from the equivalent widths of two transitions of the same ion. Thus, we need to test whether the true equivalent width is under/overestimated by modeling multiple unresolved lines with a single unresolved line.

In XSPEC, we simulate (fakeit) mock spectra by modeling the continuum with absorbed power law and O VII Kα and O VII Kβ transition each as the sum of two unresolved Gaussian absorption lines. Thus the input model is tbabs×(powerlaw + zagauss$_{K\alpha,1}$ + zagauss$_{K\beta,1}$ + zagauss$_{K\alpha,2}$ + zagauss$_{K\beta,2}$). The flux of the continuum is set sufficiently large to keep O VII Kβ detectable in all spectra. We use the response file and auxiliary file of one of our ACIS/LETG data.

Each Gaussian (zagauss) is characterized by wavelength (λ), redshift (z), broadening (b), and amplitude (a). The wavelengths of the Gaussians are set at the z=0 wavelengths of O VII Kα and O VII Kβ transitions. The line-of-sight (LOS) velocity that determines the redshift is kept within the velocity resolution (≈300 km s^{-1}) so that it is unresolved from z=0. Because O VII is detectable in the temperature range of ≈ $10^{5.4-6.4}$ K (see ionization fraction of O VII in Fig. 1, right panel), the line broadening is set to be similar to the thermal broadening in this temperature range, i.e., 16–51 km s^{-1}. The line broadening and LOS velocity of the two Gaussians of the same transition are allowed to be the same or different. The amplitude of the first Gaussian, a$_1$, is set such that
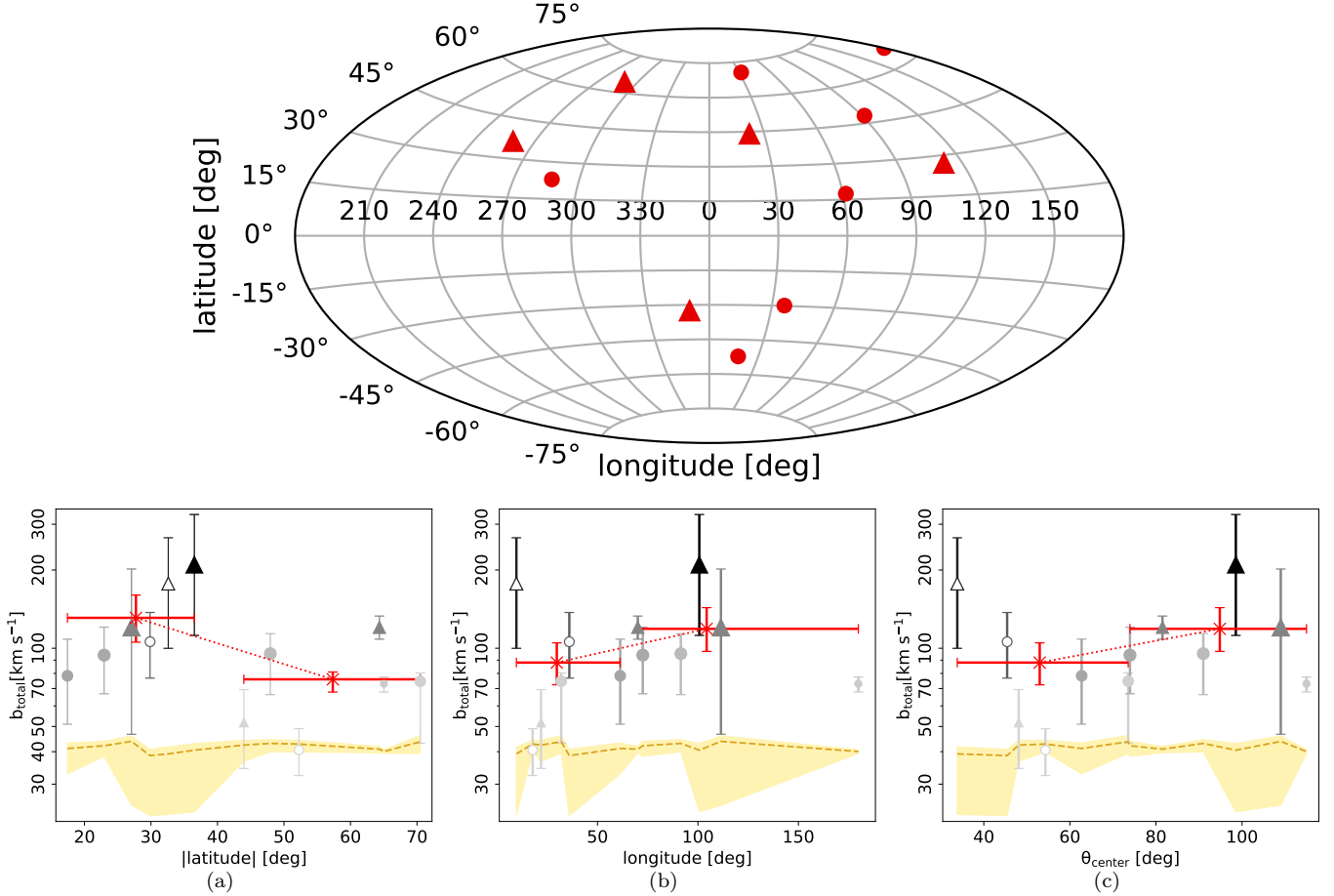
Figure 3. Top: Sky distribution of the sightlines, with *Chandra* and *XMM-Newton* data shown with circles and triangles. Bottom: O VII line broadening at different galactic latitudes (left), longitudes (middle), and angle from the Galactic center, $\theta_{\rm center}$ (right). The binned line broadening is shown with the red points. The grayscale symbols' size, shape, and shades are the same as Fig. 2. Sightlines in the southern hemisphere ($b < 0$) are shown with unfilled symbols. The thermal broadening is shown with the dashed brown curves and the yellow-shaded region. Non-thermal line broadening is evident toward sightlines at lower galactic latitudes. The correlation between non-thermal line broadening and galactic longitude or $\theta_{\rm center}$ is weak/negligible.

the resulting EW is similar to the median of the measured EW toward 12 sightlines presented in this letter. We consider three amplitudes of the second Gaussian, a_2: 1)smaller, 2)equal, and 3)larger than a_1. The line broadening and LOS velocities of the two O VII Kβ lines are kept the same as those of the two O VII Kα lines. The amplitude of O VII Kβ lines is set according to the EW ratio of unsaturated O VII Kβ and O VII Kα lines (eq. 1). For each combination of amplitude, line broadening, and LOS velocity of the Gaussian lines, we create 100 mock spectra. The normalized unfolded spectra are shown in Fig. 4a.

Next, we fit each simulated spectrum in `XSPEC` by modeling O VII transitions with one unresolved Gaussian absorption line: `tbabs`×(`powerlaw` + `zagauss`$_{{\rm K}\alpha}$ + `zagauss`$_{{\rm K}\beta}$). We turn Bayesian inference on and consider the fit statistic of c-stat. The LOS velocity is forced to be within the velocity resolution. The normalization, LOS velocity, and line broadening of O VII Kβ and O VII Kα lines are allowed to vary independently from

each other. We obtain the EW of O VII lines from the best-fit model for every 100 spectra that were simulated for each combination of input parameters and consider the median and 68% confidence interval of the EW distribution. The best-fitted EW ratio of the two transitions is shown in Fig. 4b.

The line broadening of the two input Gaussian lines is the same in the diagonal panels of Fig. 4a and 4b, i.e., $b_1 = b_2$. Here, the LOS velocity of those two Gaussians is the same in the yellow-shaded region. If two Gaussians of the same width are centered at the same mean value, they are equivalent to one Gaussian with its amplitude equal to the sum of those two Gaussians. Thus, the input models for these cases converge to one Gaussian line, and we can use them for consistency check, i.e., whether we can retrieve the input EW of a single Gaussian and thus verify the performance of the simulation and fit.

In the non-diagonal panels of Fig. 4a and 4b, the input Gaussian with larger line broadening could be treated
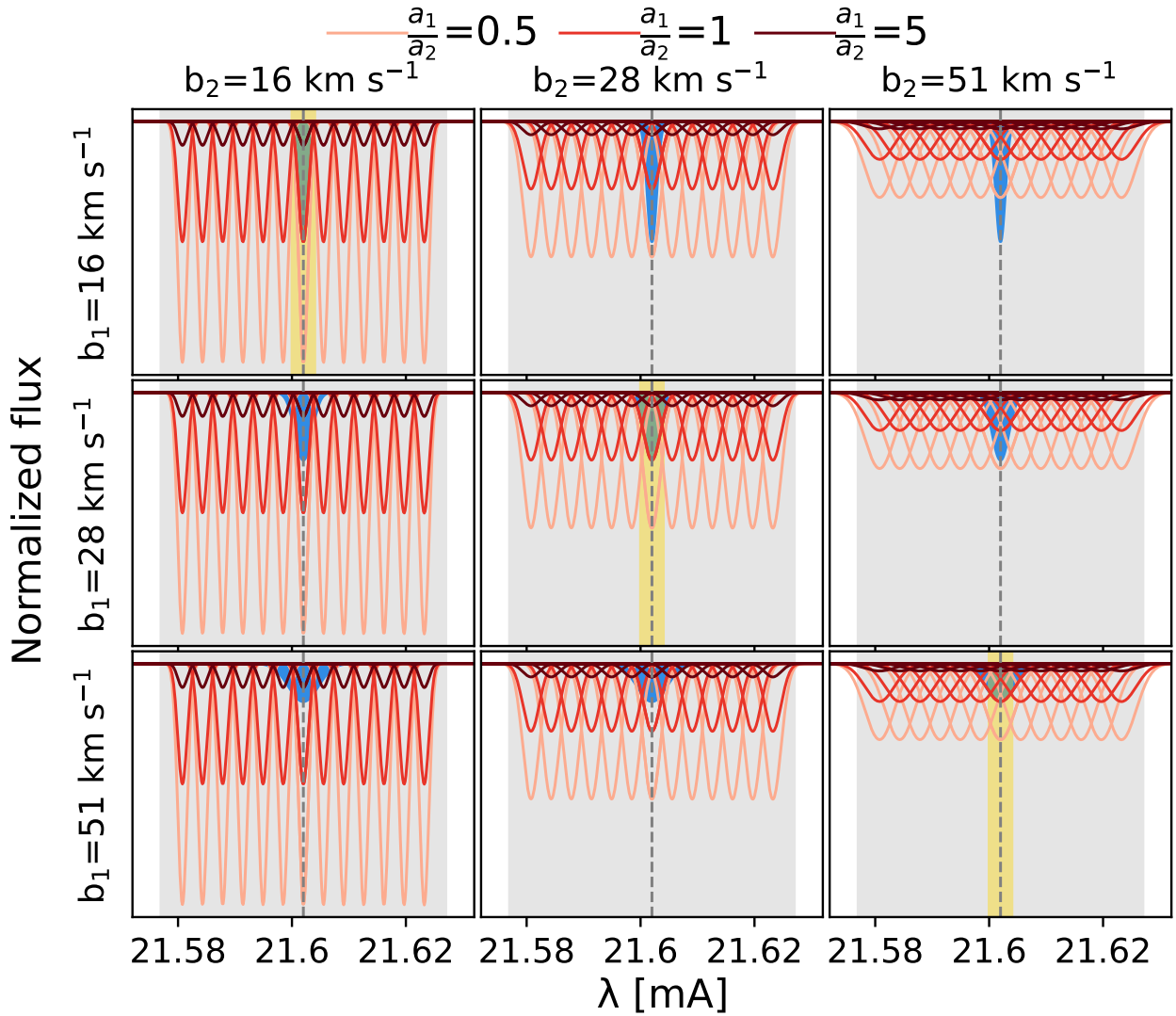
Figure 4a. Illustration of the 2-Gaussian input models for O vii Kα in simulated spectra. The yellow-shaded regions denote the subset of models where 2-Gaussian effectively converges to 1-Gaussian. The broadening of input lines in each panel is labeled on the y-axis and upper x-axis. The first Gaussian is shown in blue. Different shades of red denote 3 different amplitudes of the second Gaussian (see the legend). The second Gaussian is shown for 13 line-of-sight (LOS) velocities. For each combination of line broadening, line amplitude ratio, and LOS velocity, the input is the first Gaussian and one of the 3×13 red-shaded Gaussians. The vertical gray dashed line and the shaded region correspond to the $z=0$ wavelength of O vii Kα and the resolution element (of LETG), respectively. Models for O vii Kβ would look similar except for the amplitude of all lines being weaker.

as a purely thermally broadened line at its input temperature or a non-thermally broadened line at a lower temperature. Thus, these panels serve as lines from multiple temperatures as well as a mix of thermally and non-thermally broadened lines.

As we see, all EW ratios are consistent with the ratio of unsaturated lines. Thus, fitting two unresolved Gaussians with one unresolved Gaussian is unlikely to result in under/over-estimation of the input EW, irrespective of the LOS velocities and amplitudes of the input Gaussians. Therefore, we rule out that in our data purely thermally broadened multiple components are manifested as a single non-thermally broadened com-

ponent. Thus, we robustly confirm our detection of non-thermal broadening in the warm-hot CGM.

3.3. *Multiple temperature components*

Throughout our analysis, we have assumed that all of the O vii and O viii exist in the same phase. Based on the oxygen-only analysis, we cannot test the possibility of deviation from a single phase. However, by simultaneously studying multiple metal ions (e.g., N, Ne, Si) in addition to oxygen, a super-virial $\approx 10^7$ K hot phase co-existing with the $\approx 10^6$ K warm-hot CGM has been identified toward several individual high S/N sightlines (Das et al. 2019b, 2021; McClain et al. 2024, highlighted
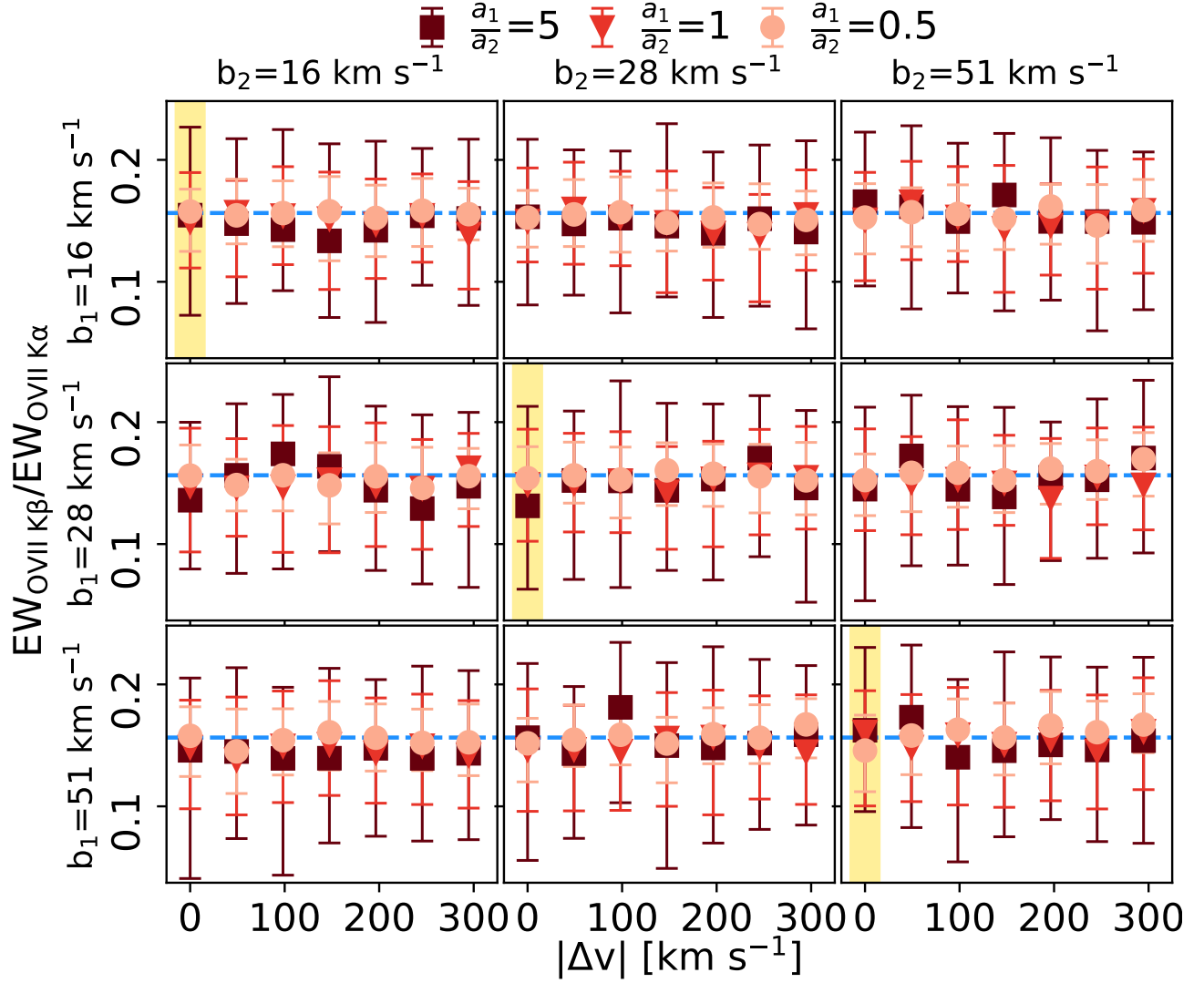
Figure 4b. The ratio of best-fitted EW of O VII Kβ and O VII Kα lines each modeled with 1-Gaussian, as a function of LOS velocity difference, $|\Delta v|$, between the two input Gaussians. Different symbols denote different amplitude ratios of the two input Gaussians (see the legend). The broadening of input Gaussians is mentioned next to each panel. The results are the same for positive and negative LOS velocity, thus effectively there are 7 $|\Delta v|$ for each combination of line broadening and line amplitude ratio. The horizontal dashed blue line in each panel corresponds to the EW ratio of unsaturated O VII lines.

in Fig. 2) and stacking of many low S/N sightlines (Lara-DI et al. 2023). In those scenarios, O VII comes predominantly from the warm-hot phase, but O VIII comes from both the hot and warm-hot phases in a comparable amount. Thus, N(O VIII) in the warm-hot phase is smaller than the total N(O VIII) measured toward those sightlines.

In this letter, the temperature is measured from the column density ratio of O VIII and O VII, and in most of the sightlines, the data is not deep enough to look for other metal lines and test the presence of a super-virial hot phase. A smaller N(O VIII) would lead to a lower temperature and hence smaller thermal broadening of oxygen lines in the warm-hot phase. As the total line broadening remains unchanged, smaller ther-

mal broadening implies larger non-thermal broadening. For example, the non-thermal line broadening toward Mrk 421 is $\approx 61\,\mathrm{km\,s^{-1}}$ assuming that a single phase contains all of O VII and O VIII. However, simultaneous hybrid-ionization modeling of O VIII-containing warm-hot and hot phases revealed that the non-thermal line broadening of the warm-hot CGM is $\approx 200\,\mathrm{km\,s^{-1}}$ (Das et al. 2021). Even sightlines currently without any evidence of non-thermal broadening in a single-phase scenario might have nonzero non-thermal broadening once they are more accurately characterized in a multiphase scenario with deeper data and rigorous ionization modeling. With the current data, we can qualitatively claim the detection of the effect of non-thermal sources on the warm-hot CGM.

4. SUMMARY AND CONCLUSIONS

In this letter, we present the first detection of the non-thermal line broadening in the warm-hot CGM using $z = 0$ X-ray absorption measurements of O VII and O VIII lines toward quasar sightlines. Theoretical simulations of the warm-hot CGM should include the non-thermal sources to match observations. Below, we summarize our results:

1. Non-thermal line broadening is evident in 8 out of 12 sightlines. On average, the non-thermal broadening is $\approx 50\%$ stronger than the thermal broadening. The detection of non-thermal line broadening is not correlated with the column density of O VII, O VIII, or the temperature of the warm-hot CGM measured toward these sightlines.

2. The correlation between non-thermal line broadening and the longitude of sightlines or the angle from the Galactic center is negligible. Thus, non-thermal sources from nuclear activities, if any, do not have any observable effect on the warm-hot Galactic halo.

3. Non-thermal line broadening is $\approx 74\%$ stronger toward sightlines at lower galactic latitude. This suggests that non-thermal sources affecting the warm-hot Galactic halo likely originate in the Galactic disk.

We emphasize that we have used archival data of *Chandra* and *XMM-Newton*. All the quasar sightlines were observed to study primarily the target itself or the intervening warm-hot intergalactic medium. Thus, the S/N of the data is not adjusted to the opacity of the warm-hot CGM of the Milky Way, leading to inhomogeneous detection sensitivity in the oxygen ions. Despite the limitations, the thermal and chemical characterization of the warm-hot/hot CGM in previous studies and the constraint on the non-thermal broadening in this letter show promising avenues for utilizing high-resolution spectroscopic X-ray data. Deeper observations are required toward sightlines with already detected O VII Kα line (but no other line) to detect O VII Kβ and O VIII Kα lines. It would allow us to improve the estimate of covering fraction and sky distribution of the non-thermal broadening. Surveys targeted towards CGM science with current satellites, e.g., gratings of *Chandra* and *XMM-Newton*, microcalorimeter onboard *XRISM* and proposed missions like *Arcus* and *LEM* would lead to a better understanding of the properties of the warm-hot CGM in X-ray absorption.

5. ACKNOWLEDGMENTS

Facilities: Chandra, XMM-Newton

Software: CIAO (Fruscione et al. 2006), HeaSoft (Drake 2005), Jupyter (Kluyver et al. 2016), Matplotlib (Hunter 2007), NumPy (Harris et al. 2020), SciPy (Gommers et al. 2022), XSPEC (Arnaud et al. 1999)

REFERENCES

Arnaud, K., Dorman, B., & Gordon, C. 1999, XSPEC: An X-ray spectral fitting package. http://ascl.net/9910.005

Bennett, J. S., & Sijacki, D. 2020, MNRAS, 499, 597, doi: 10.1093/mnras/staa2835

Das, S., Mathur, S., Gupta, A., & Krongold, Y. 2021, ApJ, 918, 83, doi: 10.3847/1538-4357/ac0e8e

Das, S., Mathur, S., Gupta, A., Nicastro, F., & Krongold, Y. 2019a, ApJ, 887, 257, doi: 10.3847/1538-4357/ab5846

Das, S., Mathur, S., Nicastro, F., & Krongold, Y. 2019b, ApJL, 882, L23, doi: 10.3847/2041-8213/ab3b09

Draine, B. T. 2011, Physics of the Interstellar and Intergalactic Medium (Princeton University Press)

Drake, S. A. 2005, in X-Ray and Radio Connections, ed. L. O. Sjouwerman & K. K. Dyer (Santa Fe, New Mexico: NRAO), 6.01

Fang, T., Buote, D., Bullock, J., & Ma, R. 2015, ApJS, 217, 21, doi: 10.1088/0067-0049/217/2/21

Fielding, D. B., Tonnesen, S., DeFelippis, D., et al. 2020, ApJ, 903, 32, doi: 10.3847/1538-4357/abbc6d

Fruscione, A., McDowell, J. C., Allen, G. E., et al. 2006, in Society of Photo-Optical Instrumentation Engineers (SPIE) Conference Series, Vol. 6270, Society of Photo-Optical Instrumentation Engineers (SPIE) Conference Series, 62701V, doi: 10.1117/12.671760

Gommers, R., Virtanen, P., Burovski, E., et al. 2022, scipy/scipy: SciPy 1.8.0, v1.8.0, Zenodo, Zenodo, doi: 10.5281/zenodo.595738

Gupta, A., Mathur, S., Kingsbury, J., Das, S., & Krongold, Y. 2023, Nature Astronomy, 7, 799, doi: 10.1038/s41550-023-01963-5

Gupta, A., Mathur, S., Krongold, Y., Nicastro, F., & Galeazzi, M. 2012, ApJL, 756, L8, doi: 10.1088/2041-8205/756/1/L8

Harris, C. R., Millman, K. J., van der Walt, S. J., et al. 2020, Nature, 585, 357, doi: 10.1038/s41586-020-2649-2

Heesen, V., Whitler, L., Schmidt, P., et al. 2019, A&A, 628, L3, doi: 10.1051/0004-6361/201936046

Heesen, V., O'Sullivan, S. P., Brüggen, M., et al. 2023, A&A, 670, L23, doi: 10.1051/0004-6361/202346008

Henley, D. B., Shelton, R. L., Kwak, K., Joung, M. R., & Mac Low, M.-M. 2010, ApJ, 723, 935, doi: 10.1088/0004-637X/723/1/935

HI4PI Collaboration, Ben Bekhti, N., Flöer, L., et al. 2016, A&A, 594, A116, doi: 10.1051/0004-6361/201629178

Hunter, J. D. 2007, Computing in Science and Engineering, 9, 90, doi: 10.1109/MCSE.2007.55

Ji, S., Chan, T. K., Hummels, C. B., et al. 2020, MNRAS, 496, 4221, doi: 10.1093/mnras/staa1849

Kluyver, T., Ragan-Kelley, B., Pérez, F., et al. 2016, in Positioning and Power in Academic Publishing: Players, Agents and Agendas, ed. F. Loizides & B. Schmidt, IOS Press, 87 – 90. https://ebooks.iospress.nl/publication/42900

Lara-DI, A. J., Mathur, S., Krongold, Y., Das, S., & Gupta, A. 2023, ApJ, 946, 55, doi: 10.3847/1538-4357/acbf40

Mathur, S. 2022, in Handbook of X-ray and Gamma-ray Astrophysics. Edited by Cosimo Bambi and Andrea Santangelo, 59, doi: 10.1007/978-981-16-4544-0_112-1

McClain, R. L., Mathur, S., Das, S., Krongold, Y., & Gupta, A. 2024, MNRAS, 527, 5093, doi: 10.1093/mnras/stad3497

Nicastro, F., Senatore, F., Krongold, Y., Mathur, S., & Elvis, M. 2016, ApJ, 828, L12, doi: 10.3847/2041-8205/828/1/L12

Nicastro, F., Zezas, A., Drake, J., et al. 2002, ApJ, 573, 157, doi: 10.1086/340489

Schmidt, W., Schmidt, J. P., & Grete, P. 2021, A&A, 654, A115, doi: 10.1051/0004-6361/202140920

Spitzer, Lyman, J. 1956, ApJ, 124, 20, doi: 10.1086/146200

Truong, N., Pillepich, A., Nelson, D., et al. 2023, MNRAS, 525, 1976, doi: 10.1093/mnras/stad2216

van de Voort, F., Bieri, R., Pakmor, R., et al. 2021, MNRAS, 501, 4888, doi: 10.1093/mnras/staa3938

Williams, R. J., Mathur, S., Nicastro, F., et al. 2005, ApJ, 631, 856, doi: 10.1086/431343